DEPARTMENT OF PHYSICS

PROPAGATION CHARACTERISTICS AND DISPERSION MECHANISMS OF COASTAL TRAPPED WAVES GENERATED IN SEBASTIÁN VIZCAÍNO BAY

Spridningsmekanismer och propageringsegenskaper av kustbundna vågor genererade i Sebastián-Vizcaínobukten

Amelia Thelandersson

Popular Scientific Summary

The ocean processes off the Southern California coast are of great interest to fisheries and scientists alike because of their complex nature and tendency to create a nutrient-rich environment. In studies of the movement of the sea in this area, many study the archipelago just south of the sharp turn at Port San Luis (USA); the Southern California bight (SCB) which is associated with great fluxes of nutrients. Despite it being an area of interest knowledge is lacking because of the heavy computational resources needed to replicate the remote processes affecting it. Recent studies have found that motions may be originating from Mexico but previous models of the area focus only on the coastal features of the USA.

Many kilometres further south, off the coast of Baja California, Mexico, a hook-shaped bay reaches far into the Pacific Ocean onto the widening of the continental shelf. When the wind blows over this bay, Sebastían Vizcaíno Bay (SVB), there has been a reported response in the sea surface height (SSH) variability in Port San Luis. This variability is of significant importance to be able to successfully predict the motions of the ocean in the SCB. It would be of interest to be able to recreate this variability and use it as an input for a regional model to be able to decrease the needed computational resources. One of the ways this signal is transported north is with waves, and this study intends to increase the understanding of one type of wave in particular, coastal trapped wave (CTWs).

To evaluate the impact of the waves a simplified ocean computer model of the area is used and initiated by a short wind event. The effects of the bay were singled out by creating two models, one with the coastline as it is and one where the bay is removed, and subtracting the resulting signals. This was then filtered further to single out the signal from the CTWs and their general characteristics could be determined. To further understand them a second model was used, this time linear and two-dimensional to determine the makeup of the wave and to decompose it into more easily understandable structures. This resulting characterisation can now be used to facilitate understanding and enhance the results of future models. It was shown that waves are greatly affected by the changes in the topography along the coast and that as they pass the SCB they dissipate. This dissipation is spreading the energy travelling with the waves and plays a part in the surfacing of the nutrient-rich water that makes the SCB so productive.

Abstract

To accurately model the motion of water on the California Coast a wind forcing over Sebastián Viscaíno bay (SVB) needs to be applied. Previous models of the coastal water outside of California don't take the SVB into account which leads to a loss of accuracy as some of the motion originates from the bay. The motion propagating from the bay is in part expressed as coastal trapped waves (CTWs) and the aim of this project is to classify what impact the SVB has on their generation and characteristics. Two models have been generated in MITgcm (MIT general circulation model), one with the real coastline and one where the bay has been removed. They simulate a fast wind event over the area from 27°N on the Baja California Peninsula up to 35.3° N, in the Southern California Bight, using horizontally homogenous stratification and real bathymetry.

The analysis of the resulting signal is complemented with a linear model that numerically classifies linearised CTWs to find expected and allowed waves and their modal composition. The CTWs found in the model presented the following characteristics: a period of about 1.1 days, phase speeds between 1-5 m/s and wavelengths between 97-490 km. When compared to the numerical calculation the value follows similar trends and the dominating mode is determined to be mode 1, with modal weight decreasing with increasing modal number.

Phase speed and wavelength vary greatly which due to the construction of the MITgcm model is attributed to variation in topography. Abrupt variations in topography, presented as changes in slope steepness, shelf width and total depth, are associated with a local decrease in phase speed and a local displacement of energy to lower modes and to other frequencies. Due to a lack of knowledge of the linear model's performance on complex topography, an investigation on a smoother coastline could lead to better performance. Further investigation may benefit from considering the effect of variations in friction, wind and stratification.

Contents

1 Introduction

Off the coast of Baja California, Mexico, a hook-shaped bay reaches far into the Pacific Ocean onto the widening of the continental shelf. This bay, Sebastían Vizcaíno Bay (SVB), significantly affects large-scale physical processes in the area [Wyllie, 1961, Amador-Buenrostro et al., 1995] and signals originating from the bay have been shown to affect processes further north [Pringle and Riser, 2003]. In fact, Verdy et al. [2014] found that to explain sea surface height (SSH) variability in Port San Luis (California, USA) a wind forcing over the bay, some 900 km further south, was needed.

Just south of Port San Luis, turning the sharp edge at Point Conception one finds the Southern California Bight (SCB), reaching as far south as San Diego and the Santa Rosa Ridge to the west. This area is characterised as a part of the California Current System (CCS) which has been extensively studied. Summaries of the governing physical processes can be found in multiple papers, eg. Hickey [1979]. The SCB is one of the areas of the CCS with strong upwelling, giving it biological and ecological importance due to the resulting high levels of primary production [McClatchie, 2016]. Despite this, the models of physical processes in the SCB are not yet comprehensive for effects caused by remote forcing [Dong et al., 2009, Verdy et al., 2014, Pringle and Riser, 2003, Mazloff et al., 2020]. The area is usually modelled regionally with the edges tending to be drawn at the border between the USA and Mexico, consequently excluding coastline features further south.

It is often preferred to use regional models where the surrounding conditions are input instead of a more computationally demanding global model representing the complete field without boundaries [Feser et al., 2011]. This is because the regional model can, with the proper input conditions, achieve results with higher resolution while using fewer resources compared to a global one. Trouble arrives when the knowledge of the physical state of surrounding areas is lacking, such as the case of the effect of the SVB.

The research inspiring the investigation of this particular area is presented in Mazloff et al. [2020], who have investigated the difference in the California Bight internal wave field when forced with a regional compared to a global model. The purpose was to classify what a model misses when not including influences from its surroundings. Mazloff et al. [2020] noticed that the regional model had low internal wave energy compared to the global model. This was diagnosed as an issue that can be solved by adding the internal wave energy at the boundaries while designing the model. Although the input would demand varying precision depending on the purpose of the model, Mazloff et al. [2020] states that some type of method must be established to account for internal waves.

Knowing that regional models of the SCB need the incorporation of remotely forced internal waves, the next step is to determine the characteristics of these waves. Through an adjoint sensitivity analysis Verdy et al. [2014] has named some of the effects of remote forcings on the SCB. They found that remote winds over the SVB generate the majority of the variation on longer time scales and that this effect arrives at the SCB through coastal trapped waves (CTWs). These waves link processes occurring in the SVB to the SCB by transporting temperature variations and wind effects from the bay northward. Similar connections have been noted when investigating in situ data [Pringle and Riser, 2003]. There is also evidence that CTWs are one of the key mechanisms behind the generation of the California Undercurrent (CUC), one of the governing motions of the CCS [Philander and Yoon, 1982, McCreary and Lighthill, 1981]. The classification of the behaviour of these waves is therefore of great importance as this current is responsible for a significant amount of the transportation of nutrient-rich and oxygen depleted bottom water along the west coast of the United States [Zaba et al., 2021].

Coastal trapped waves are often generated by alongshore wind stress which excites the ocean [Connolly et al., 2014, Huthnance et al., 1986, Brink, 1991]. The response to this wind in idealized models of shelf regions with homogenous water and varying bottom topography is the generation of barotropic shelf waves (also called topographic Rossby waves). If instead the region is stratified but has no variation in bottom topography the waves generated are internal Kelvin waves [Woodham et al., 2013, Wang and Mooers, 1976, Hughes et al., 2019, Enfield and Allen, 1983]. In reality, the ocean behaves like a hybrid of these two approximations, which generates what is known as coastal trapped waves (CTW). CTWs propagate with the coast on their right (left) in the northern (southern hemisphere) and can be generated by a number of phenomena such as atmospheric pressure changes, wind stress and eastward propagating equatorial waves reaching the coast. Since atmospheric events have largely varying time scales, from local storms [Enfield and Allen, 1983] to hurricanes [Zamudio et al., 2002] to phenomena such as El Niño [Colas et al., 2008], so do the generated CTWs. They also vary greatly due to factors such as depth, latitude and stratification [Wang and Mooers, 1976].

Since the 1970s the capacity to create analytical solutions encompassing all the complexity of CTWs has been expanded and today there exists a consensus for the classification of these waves. The governing equations and other forms of classification are discussed further in Huthnance et al. [1986] and Clarke and Brink [1985]. What is important to know for the understanding of these papers is that these waves can, just like any wave, be decomposed into modes, the infinite amount of frequencies that make up the wave that we see. The concept of modes is explained by visualising a string that is displaced from its original state. Whatever shape the rope takes on is called its modal structure, the order of the mode is normally defined as the amounts of nodes (times the string crosses its static state) on the string. These modes are independent of each other and one can not be a combination of the others [Georgi, 1993].

2

Calculating the free wave solution in a shelf region with arbitrary stratification results in a first mode similar to a barotropic Kelvin wave and an infinite set of higher modes of increasingly complicated structures [Brink, 1991]. The simple lower modes can be used to approximate the behaviour of the entire wave, as they dominate the wave structure, which facilitates the understanding of the wave. In a 2D wave in the ocean, presented for example as the vertical structure of the cross-shore pressure anomaly field, mode order is defined as the number of times the pressure value crosses zero. The stronger the stratification, the faster the modes propagate until they reach the inertial frequency where coastal trapped waves no longer can exist.

In this study I intend to clarify and increase the current understanding of the impact that the CTWs generated at SVB have on the physical processes on the coast of northern Baja California up to the Southern California Bight. The intention is to classify the characteristics of these waves, such as phase speed, period and wavelength, how they propagate up the coast and how they evolve as they travel north. This is done to supply information about how this wave phenomenon can be included in predictions without having to use an excessively demanding global model. The characterisation will be enhanced by evaluating linear CTW theory [Brink, 2018] in the domain. The linear theory will be applied with caution and its agreement with the developed MITgcm (Massachusetts Institute of Technology General Circulation Model) model [Marshall et al., 1997] will be assessed. A previous test on an idealised coastline shows that the response in MITgcm with the same input presents the same characteristics as that of the linear model [Musgrave, 2019]. The linear model has been applied extensively and successfully to idealised and very smooth topography [Lüdke et al., 2020, Brunner et al., 2019, Masoud et al., 2019, Battisti and Hickey, 1984, Enfield and Allen, 1983]. There are fewer applications on complex topography and its proficiency is deemed to be quite poor in accounting for all the intricate processes that a real coastline induces, e.g. scattering [Brunner et al., 2019].

To evaluate these questions this thesis begins in section 2 with a description of the configuration of the model, constructed in MITgcm. Then in section 2.2 the linear theory, which will be referred to as the linear CTW model, is described and section 2 ends with a description of how these two models will be compared. Section 3 examines the output from the MITgcm model, acknowledges the presence of a CTW signal and establishes the characteristics of this. The results section continues with an evaluation of the linear CTW model and a visualisation of the vertical modal structures allowed in the domain. Section 3 finishes off with a linear regression to determine the modal composition of the wave signal found in the MITgcm model. Finally, section 4 reviews the characteristics of these waves, comparing them to the previous theory and concludes the significance of the results.

2 Methods

2.1 Circulation model (MITgcm)

To simulate the response to the presence of Sebastían Vizcaíno Bay (SVB) two models were configured in the general circulation model MITgcm [Marshall et al., 1997]. The only difference between the models was the presence or absence of the SVB. Both encompassed the domain from northern Baja California in Mexico (27°N and 114°W) up to Port San Luis in the United States (35.3°N and 122°W) (figure 1).
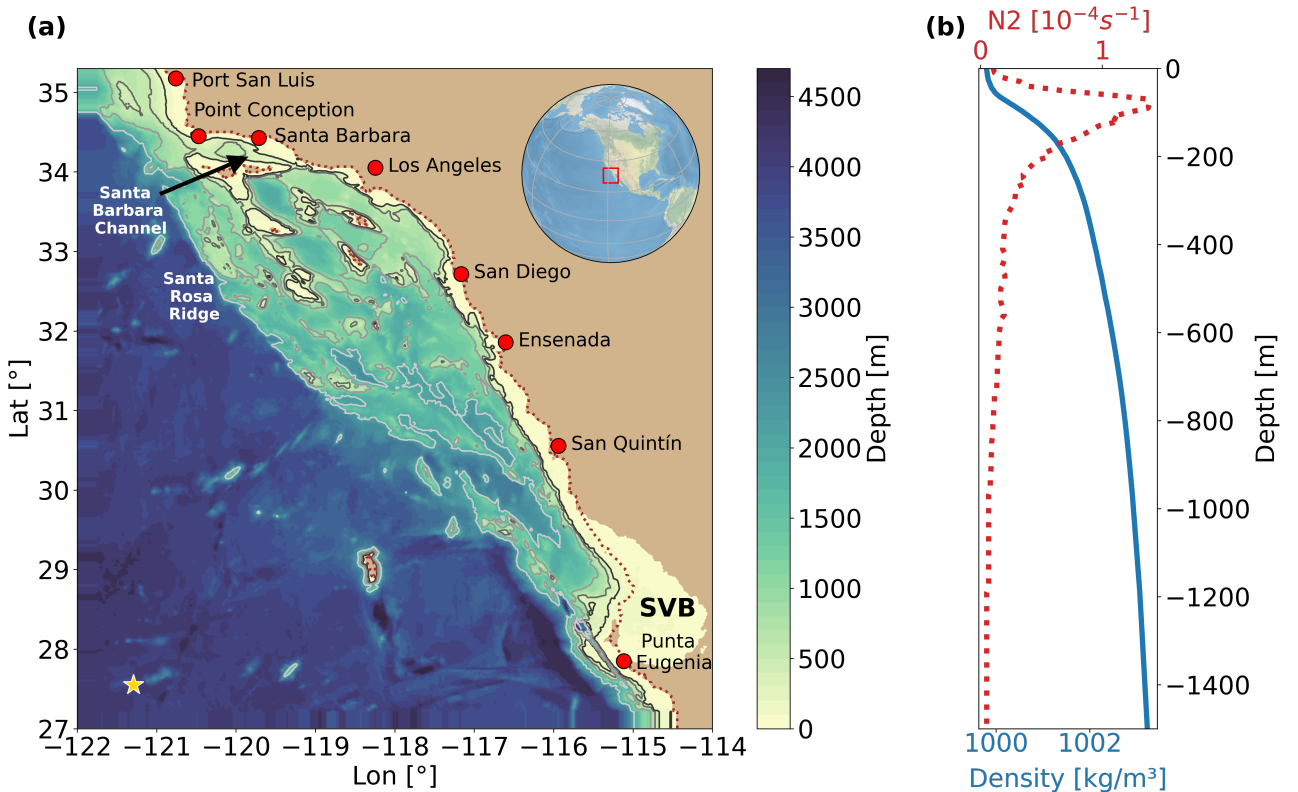
Figure 1: (a) Bathymetry and location for the model, the brown dotted line corresponds to the 150 m isobath where the coastline was drawn for the model without Sebastian Vizcaíno Bay. The star marks the location where the salinity and temperature profiles were taken from the CASE-STSE model. From these profiles, the density (b) (blue) and buoyancy frequency, N^2, (b)(red, dotted) for the model were calculated.

The real bathymetry from GEBCO Group [2020] was used to represent the bay as accurately as possible (figure 1a). The bathymetry was smoothed lightly, using ROMSTOOLS [Penven et al., 2008] which consists of one selective filter to reduce the presence of seamounts in the deep sea and a single pass Hanning filter to remove 2D noise in the topography. In the model where the bay is not present the coastline is drawn at the cross-shelf slope at 29.8°N at the 150 m isobath and followed south to Punta Eugenia, see brown dotted line in figure 1a.

The domain was divided into 512x612 cells horizontally giving a resolution of $\Delta x = 0.016°, \Delta y = 0.014°$ which is 1.5 km $\pm 10\%$. In the vertical, it was set to 100 grid points with a maximum depth of 4700 m. The vertical resolution was set to decrease with depth starting with a cell size of 2 m at the surface and down to 4700 m depth the cell size increased to 270 m thus adjacent vertical separations were set to differ by less than 10%. The boundaries were set to be open to the north, south, and west with Orlanski radiation conditions [Orlanski, 1976] and free slip boundary conditions on the sides and bottom of the basin. The 15 grid cells adjacent to the open boundaries were flattened to remove topography gradients across these boundaries.

Stratification was defined by calculating the typical values for February 2008 at 121.3°W, 27.6°N (star in figure 1a shows this location and in figure 1b the resulting stratification is shown) from the California State Estimate (CASE-STSE). It was set to be horizontally homogenous over the domain and was resolved so the depth spacing had the maximum density increments of 0.08 to 0.15 kgm^{-3} where the depth cell size is 2 m. The evolution of the stratification follows a linear equation of state with coefficients for thermal expansion $\alpha_T = 2.0 \times 10^{-4}°C^{-1}$ and for haline contraction $\beta_S = 7.4 \times 10^{-4}$ kgg^{-1}. Dissipation and diffusive fluxes change according to vertical (subscript z) and horizontal (subscript h) diffusivity (K) and viscosity (A) coefficients:

$A_h = K_h = 100$ ms^{-2}
$A_z = K_z = 10^{-5}$ ms^{-2}.

An initial perturbation was created by applying a spatially homogeneous alongshore wind stress over the whole domain. It was set to be parallel to the coast of Baja California with direction -30°N, blowing to the southeast. It develops according to the first half of the Gaussian function:

$$\tau_{\parallel} = [1 - H(t - t_c)]\tau_{max}e^{-\frac{(t-t_c)^2}{2\sigma}} \tag{1}$$

where $H(t)$ is the Heaviside step function, $t > 0$ is time and $t_c = 3.5$ hr is the time when forcing reaches the maximum value, $\tau_{max} = 0.1$ Nm^{-2} and $\sigma = 1$, at which point the forcing stops. This was done to create a realistic but simple representation of the wind forcing. For further information on the wind estimate, refer to Ramos-Musalem [Under review]

The model was then left to oscillate freely for a time span of 10 days with a time step of 60 s and outputs every 10 minutes the first 5 days and the remaining days every 20 minutes.

The run without the bay was subtracted from the one with the bay to filter out signals not generated by the presence of the bay. Further filtering of signals not within the spectrum of CTWs was performed with a sixth-order Butterworth bandpass filter with frequency cutoffs at 1/0.5 and at 1/5 days. To remove geostrophic adjustment the signal was linearly detrended over time.

2.2 Coastal trapped wave model

For each run, expected and allowed waves were numerically calculated at different transects along the coast and compared to the signals found in the MITgcm configuration. The calculations were performed using code shared by Kenneth Brink [2018]. This model and its predecessors have been used extensively and successfully in predicting allowed coastal trapped waves [Eg. Lüdke et al., 2020, Brunner et al., 2019, Masoud et al., 2019, Battisti and Hickey, 1984, Enfield and Allen, 1983]. It was produced to classify linearised coastal trapped waves for real, sub-inertial frequencies. The theory used in the code is explained briefly below while further information can be found in documents provided by Brink [2018] and cited sources therein.

For a coastline uniform in the alongshore direction the following equations of motions are applied, assuming hydrostatic conditions

$$v_t + uv_{0x} + v_0v_y + wv_{0z} + fu = -\rho_0^{-1}p_y + \rho_0^{-1}\tau_z^y \tag{2a}$$

$$\delta u_t + \delta v_0 u_y - fv = -\rho_0^{-1}p_x + \delta\rho_0^{-1}\tau_z^x \tag{2b}$$

$$0 = -p_z - g\rho_2 \tag{2c}$$

$$u_x + v_y + w_z = 0 \tag{2d}$$

$$\rho_{2t} + u\rho_{1x} + v_0\rho_{2y} + w\rho_{1z} = 0, \tag{2e}$$

where the subscripts represent partial differentiation, u, v, w are the perturbation velocity components in the x, y, z directions, respectively, p is perturbation pressure, f is the Coriolis parameter, density is decomplied as $\rho_0 + \rho_1(x, z) + \rho_2(x, y, z, t)$ where $\rho_0 >> \rho_1 >> \rho_2$. Using $\delta = 1$ corresponds to a general frequency and wavenumber, while $\delta = 0$ produces the long-wave limit, and only allows one frequency to be computed. τ^x and τ^y are turbulent stresses in the x, and y directions, respectively used for computing the damping coefficients after the inviscid wave mode is known.

A free wave solution is sought in the form

$$p = p'(x, z)e^{i(\omega t + ly)}, \tag{3}$$

here shown for the pressure variable, only allowing real frequencies, ω, and wavenumbers, l. With these assumptions and expressing density gradients in terms of the Brunt–Väisälä frequency, the problem is reduced to a single partial differential equation, dropping the primes

$$0 = \omega' p_{xx} - 2\omega' s p_{xz} + \omega' N^{-2}(ff' - \delta\omega'^2)p_{zz} - \omega'(Q + s_z)p_x -$$
$$[-\omega' sQ + (\omega' s)_x + lf^{-1}s(f^2 - \delta\omega'^2) - (\omega' N^{-2})_z(ff' - \delta\omega'^2) - (\omega' N^{-2})(sM^2)_z]p_z - \quad (4a)$$
$$[lfQ + \delta\omega' l^2 + lfs_z]p,$$

where

$$\omega' = \omega + lv_0 \quad (4b)$$

$$s = \frac{M^2}{N^2} \quad (4c)$$

$$M^2 = -\frac{g}{\rho_0}\rho_{1z} \quad (4d)$$

$$N^2 = -\frac{g}{\rho_0}\rho_{1x} \quad (4e)$$

$$f' = f + v_{0x} \quad (4f)$$

$$Q = (ff^* - \delta\omega'^2)^{-1}[(ff^* - \delta\omega'^2)_x - s(ff^* - \delta\omega'^2)_z] \quad (4g)$$

$$f^* = f + v_{0x} - \frac{M^2 s}{f}. \quad (4h)$$

Equation 4a is then solved in the code through resonance iteration.

As input, the same bathymetry transects and stratification were used as in the MITgcm model (figure 1). The code was applied to multiple cross-sections of interest searching for general solutions, not within the long-wave limit, as it restricts the solution to alongshore scales being much larger than cross-shore scales which we cannot deem to be the case here. Further input included the boundary conditions which were defined as an open offshore boundary and a closed onshore boundary with a free surface. Grid sizes were set following the limitation of a hydrostatic consistency ratio under 8, calculated as $\frac{h_x \Delta x}{h \Delta \theta}$, where h is depth, h_x is the partial derivation of depth with respect to x, Δx is the difference is cross-shore distance, and $\Delta\theta$ is the difference in $\theta = z/h(x)$. Thus the grid points in z are set to 20 and, depending on the steepness of the shelf slope, the grid points in x are set between 200-600. Encompassing a distance from the shore of 100 km the resolution in x is between 0.167-0.5 km and the resolution in z depends on total depth but varies between 40-150 m, where the resolution is the same over the whole cross-section. The open offshore boundary condition requires a flat bottom which was set by smoothing topographical changes at the edge of the model (Eg. compare topography in figure 6a with c-g). This smoothing was applied in a few different ways but results from the different methods had no large variation, and the most efficient way was thus chosen. Bottom friction was set constant to be proportional to an alongshore flow of size 0.05 cm/s and the initial alongshore flow was set to zero. The code requires a guess at the frequency of the wave, and attempts were carried out with a guessed frequency between 1/0.5

to 1/5 days. These were the preliminary values of the frequency of the wave observed in the MITgcm model. It also requires an expected wave number which was the parameter changed to find the different wave modes, where a higher wavenumber resulted in a higher mode number.

Equation 4a is then solved through resonance iteration using the previously mentioned inputs and the model outputs the structures of u, v, w, density, and pressure, along with energy diagnostics, wavenumber, friction damping coefficient, frictional decay and frequency. Units are given in the centimetre–gram–second system of units (C.G.S).

2.3 Comparison between the models

2.3.1 Wave characteristics

In the output data from the MITgcm model the phase speed of the wave was determined using lagged correlations between a set of points distributed evenly every 100 km along the coast (see figure 3c for the starting point which is the southernmost point either red, for SSH, or black, for vertical velocity). The power spectral density (PSD) was calculated along the coast using a one-dimensional Discrete Fourier Transform (DFT) based on Fast Fourier Transform (FFT). By determining at what frequencies the PSD was highest the frequency and period of the waves were found. From this, the wavelength and wavenumber were determined.

With the output from the CTW model wavelength and phase speed could be determined using the well-known formula $c_p = \omega/k = \lambda/T$, where c_p is the phase speed, ω is the angular frequency, k is the wavenumber, λ is the wavelength and T is the period of the wave. These outputs are given for specific modes while the ones from the MITgcm model are determined for a complete wave, with all modes coexisting. This means that these values could only roughly determine the agreement between the models.

2.3.2 Linear regression

A linear relationship was assumed between the vertical structures of the waves in the MITgcm model and those of the modes in the linear model. Under this assumption, multivariate linear regression was applied to the data to project the contribution of each mode in the structure observed in the MITgcm model. Using the vertical structure of pressure from both models the weight of the different modes was determined. The method applied was a least squares fit which will be explained in short here following the theory of Thomson and Emery [2014].

The goal was to fit a dependent model parameter of size N, $y_i(i = 1, 2, \ldots, N)$, in this case the resulting structure from the MITgcm model, to an M number of independent variables $x_{ij}(j = 1, 2, \ldots, M)$, each variable being a mode from the CTW model. This is done by seeking

the parameters b_j that best fit the function: $\hat{y}_i = b_0 + b_j x_{ij} + \epsilon_i$, where the hat denotes that it is an estimate, ϵ is the error and x_{i0} is an adjustment vector of ones. The error is the variance obtained by a linear regression. By calculating the sum of squared errors $SSE = \sum_{i-1}^{N} \epsilon^2$, one can find the values of b with the smallest error thus when the partial derivative of the following equation with respect to b is equal to zero

$$SSE = \sum_{i=1}^{N} [y_i - (b_0 + b_j x_{ij})]^2. \tag{5}$$

Solving this results in

$$\hat{b}_j = \frac{[N \sum_{i=1}^{N} x_{ij} y_i - \sum_{i=1}^{N} x_{ij} \sum_{i=1}^{N} y_i]}{[N \sum_{i=1}^{N} x_{ij}^2 - (\sum_{i=1}^{N} x_{ij})^2]} \text{ and in turn } \hat{b}_0 = \bar{y} - \hat{b}_j \bar{x}_{ij}, \tag{6}$$

where the hat represents an estimate. In this study it can preferably be expressed in a matrix form where x_{ij} is the element in the i-th row and j-th column of the $\mathbf{X}$ matrix, b_j is the element in the j-th column of the $\mathbf{B}$ vector (where b_0 is placed in the 1st column of $\mathbf{B}$ and the 1st column of $\mathbf{X}$ is set as an i number of ones) and ϵ_i and y_i are the i-th elements of the $\mathbf{E}$ and $\mathbf{Y}$ vectors, respectively. The equation can then be expressed as: $\mathbf{Y} = \mathbf{B} \cdot \mathbf{X} + \mathbf{E}$. Solving for $\mathbf{B}$ using ordinary least squares provides the solution

$$\mathbf{B} = (\mathbf{X}^T \cdot \mathbf{X})^{-1} \mathbf{X}^T \cdot \mathbf{Y}. \tag{7}$$

This technique was used on vertical structures for the allowed modes that were encountered. Prior to the linear regression, the vertical structures from the CTW were interpolated, using a 2D linear interpolation, to fit the dimensions of the MITgcm output. The resulting weights were multiplied with the vertical structure for their respective mode and then added with the intention to recreate the vertical structure from the MITgcm output. This gives the weight of each mode and insight into which mode dominates at different times and locations along the coast.

3   Results

3.1   CTW characteristics in the circulation model

A CTW signal is present in the domain, propagating northward along the coast from the bay and it is visible as a positive anomaly followed by a negative anomaly in figure 2. The signal is shown for days 2, 4 and 8 in filtered SSH in figure 2a, c and e and in the unfiltered vertical velocity field at depth 480 m in figure 2b, d and f. In vertical velocity, the signal being unfiltered, we also see higher-frequency waves in this signal that dissipate with time, just as the amplitude of the CTW signal (compare figure 2a, d and e). The signal propagates northward

9

with the coast on the right. The signal at depth is clear until the Santa Barbara channel, which at 480 m depth is closed off by the topography, around 34 °N (figure 1a and 2d and e), or approximately 700 km from the bay. In signals in SSH the wave signal is present until around Los Angeles, 33°N, about 600 km from the bay (figure 3a and b). The initial trapping distance of the wave varies between 55 km in the south to 45 km in the north and decays over time with the smallest being around 5 km.

To follow the signal over time, points were taken out along the coast, see markers in figure 3c which show the location of the values every 200 km for SSH (red) and vertical velocity (black). Over this distance, the signal is presented over time in figure 3a for SSH and b for vertical velocity. A positive signal followed by a negative signal was seen over the whole time period, both in SSH and vertical velocity. The signal after 600 km in SSH and after about 700 km in vertical velocity is deemed to no longer be CTWs and therefore it is excluded from the following analysis. The slope of the signal was used to estimate the phase speed which in SSH decreases northward, seen as flattening of the slope (see values of phase speed in table 1 column 9), but the same pattern was not present in signals present in variables at depth (figure 3a-b). Instead, there were certain areas with rapid increases/decreases in phase speed, seen as steeper/flatter slopes in figure 3. The phase speed was estimated using lagged correlation between evenly spaced points, every 100 km along the coast, beginning at the southernmost black point in figure 3c. The correlation between the first point and points at 113, 337 and 562 km from this point is shown in figure 4, their maximum correlation was found at lags 0.8, 1.6 and 2.9 days, respectively. The distance was divided by the time lag between the locations and the resulting phase speed varied between 1-5 m/s. In table 1 four locations have been chosen and their characteristics are summarised.
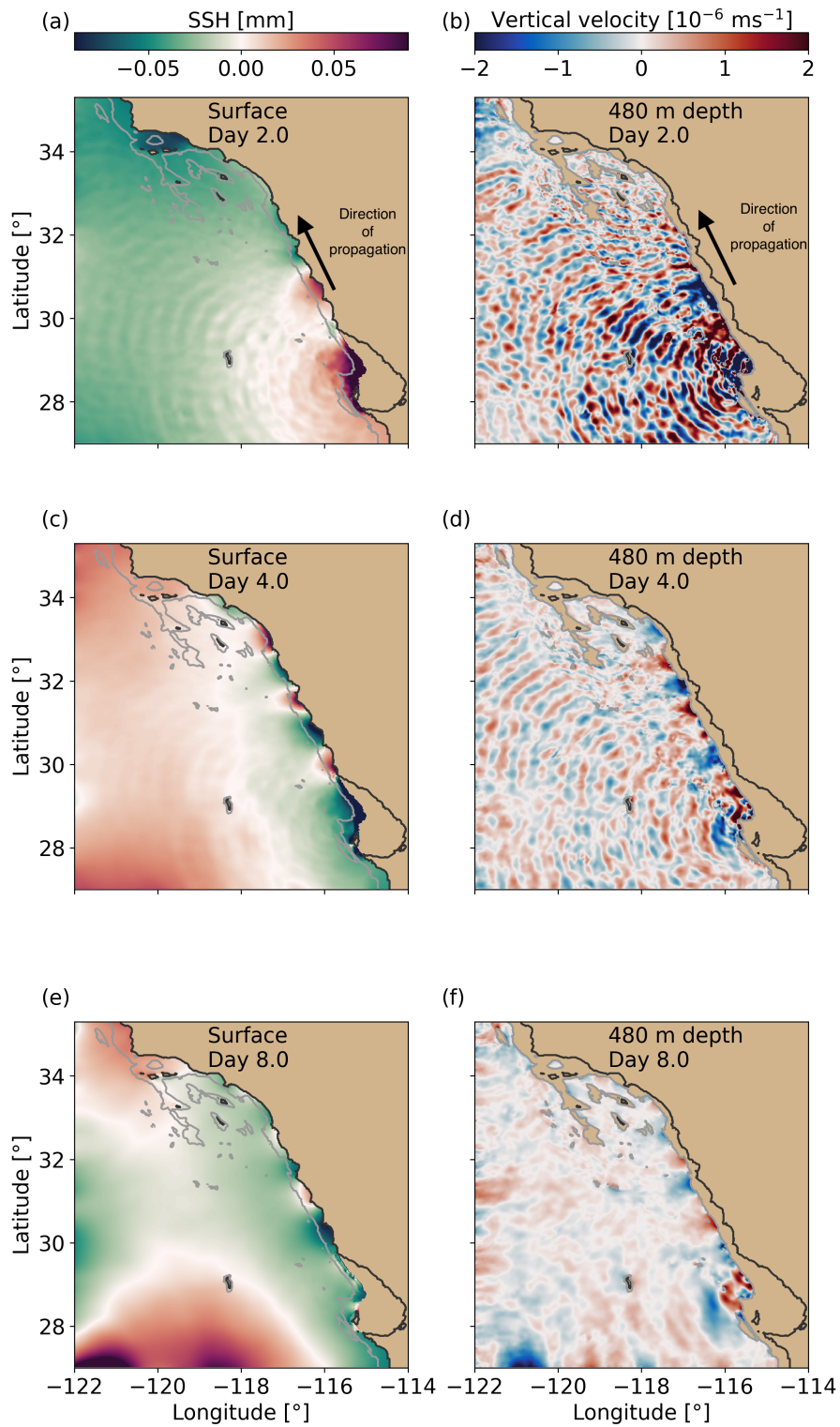
Figure 2: The resulting signal from the run without the bay being subtracted from the run with the bay shown after 2 (a), 4 (c) or 8 (e) days in filtered and detrended sea surface height and vertical velocity, unfiltered at 480 m depth, after 2 (b), 4 (d) or 8 (f) days in. The 0 m and 500 m isobaths are marked as black and grey lines respectively. An arrow marks the propagation direction.
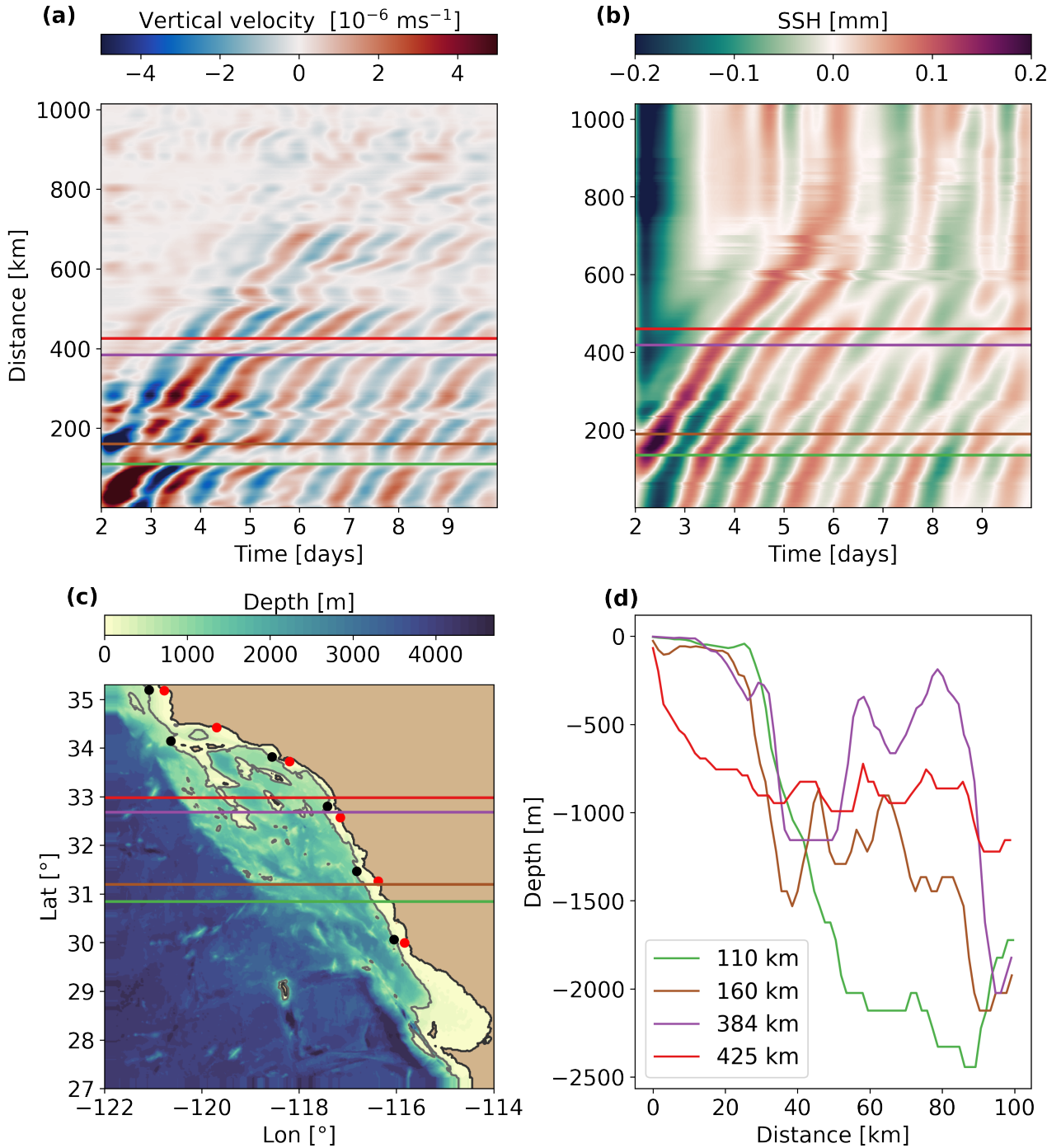
Figure 3: The resulting signal from the run without the bay being subtracted from the run with the bay of (a) filtered vertical velocity at 480 m depth and (b) filtered and detrended sea surface height. The values in (a) have been taken along the 480 m isobath which is along the light yellow coastline while the values in (b) are taken along the sand-colored coastline. In (c) dots have been placed corresponding to the distance on the y-axis, in (a) (black) and in (b) (red) beginning from 0 and then every 200 km. In (a-c) four cross sections have been marked out, and in (d) the bathymetry of these cross sections was shown, legend showing the exact distance from the distance 0 point in vertical velocity (starting from the southernmost black dot in (c)).

12
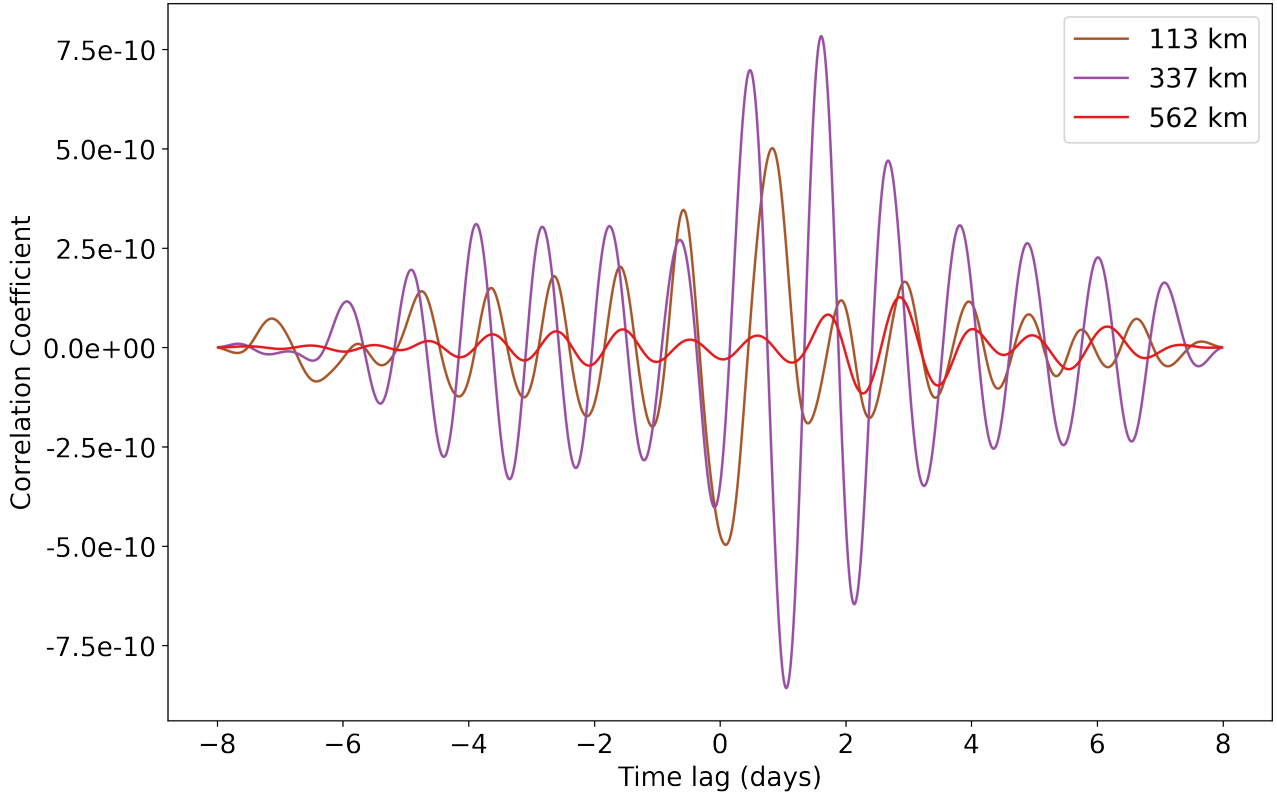
Figure 4: The lagged correlation of the vertical velocity signal between the point closest to the bay (black points in figure 3c) and three following locations, 113, 337 and 562 km from the bay. The maximum absolute correlation was found at 0.8, 1.6 and 2.9 days for 113, 337 and 562 km respectively.

From the power spectral density (PSD) analysis, the frequencies where the PSD is highest give the frequency and period of the strongest signal. After filtering, the strongest signal corresponds to the frequency of the CTWs. This method was applied to multiple variables such as pressure, density, SSH and velocities. After filtering they all presented the highest spectral density around 60 km from the bay and at frequencies corresponding to a period of 1.1 days (figure 5). This frequency is far under the inertial frequency which corresponds to a period of about 1 days.

Figure 5: The power spectral density of the vertical velocity signal, in (a) along the coast while (b) shows the cross sections marked in (a), colours corresponding.

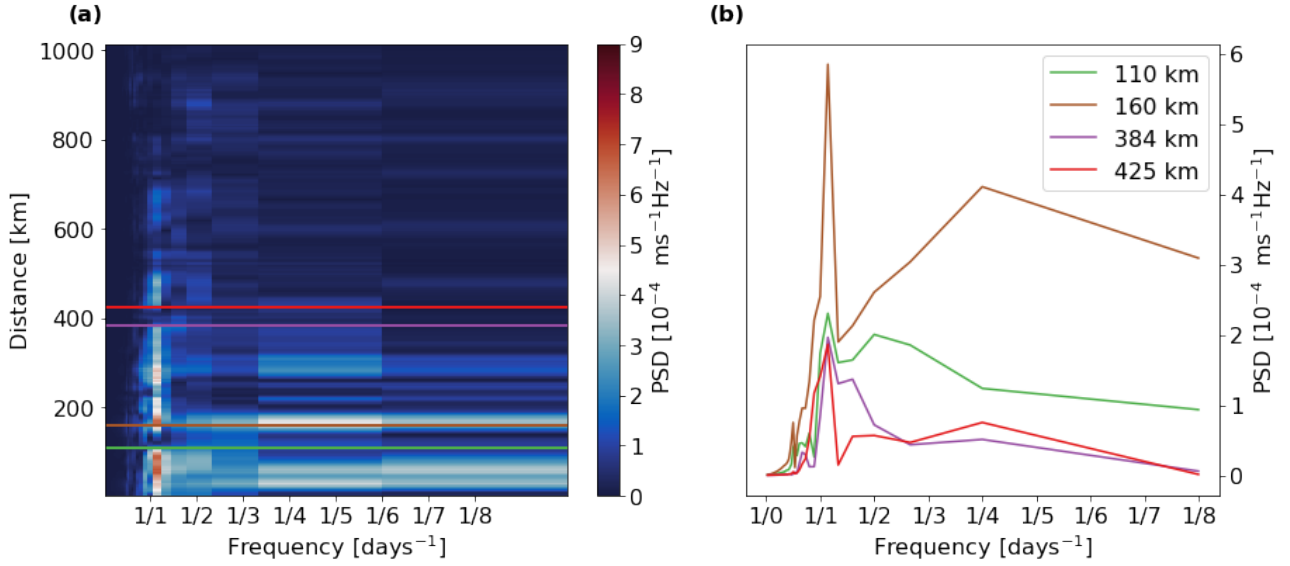With a period of 1.1 days and a phase speed varying between 1-5 m/s, the wave's wavelength is between 97-490 km. In the Hovmöller plot (figure 3) areas of increase and decrease of phase speed can be seen over relatively short distances. Two of these locations around 31° N (110-160 km from the bay) and around 32.7°N (384-425 km from the bay) have been marked out. Their corresponding bathymetry is shown in figure 3d. The same colours are used to mark these locations in figure 5a showing that they are also areas with lower power. The PSD at these points 3c is shown in 5b and here one can see an increase in energy in frequency 1/4 days^{-1} at 160 km and 425 km from the bay in comparison to 110 km and 384 respectively.

The wave characteristics for the signal at depth are shown for four locations along the coast in 1, column 8 (at depth 480 m) and 9 (at the surface).

3.2 CTW characteristics in the CTW model

The vertical pressure structure of the first five modes at a cross-section at 30.7°N is shown in figure 6. The mode number is determined by the number of zero crossings present in the pressure field. We see barotropic tendencies on the shelf, meaning the pressure gradient is vertical, and the higher the mode the more complex of a structure at depth with the wave becoming trapped to the bottom. The characteristics of the allowed modes in the domain are a period between 1.2 (barotropic mode: 0.9) - 2.5 days, and a phase speed between 0.4 - 3 (barotropic mode: 8) m/s. The phase speed can be seen as the slope of the dispersion curves which decreases with mode number while the period increases (figure 6b). The dispersion curves thus behave as expected and are limited to values far under the inertial frequency. The barotropic mode, mode 0, has been excluded as its faster phase speed would mean that at the beginning of the

14

analysis, two days after the disturbance, it would have already left the domain (8m/s ∼ 29 km/h, meaning it would take about 1.5 days to travel the whole domain of 1000 km). The resulting characteristics for four locations along the coast have been summarized in table 1.
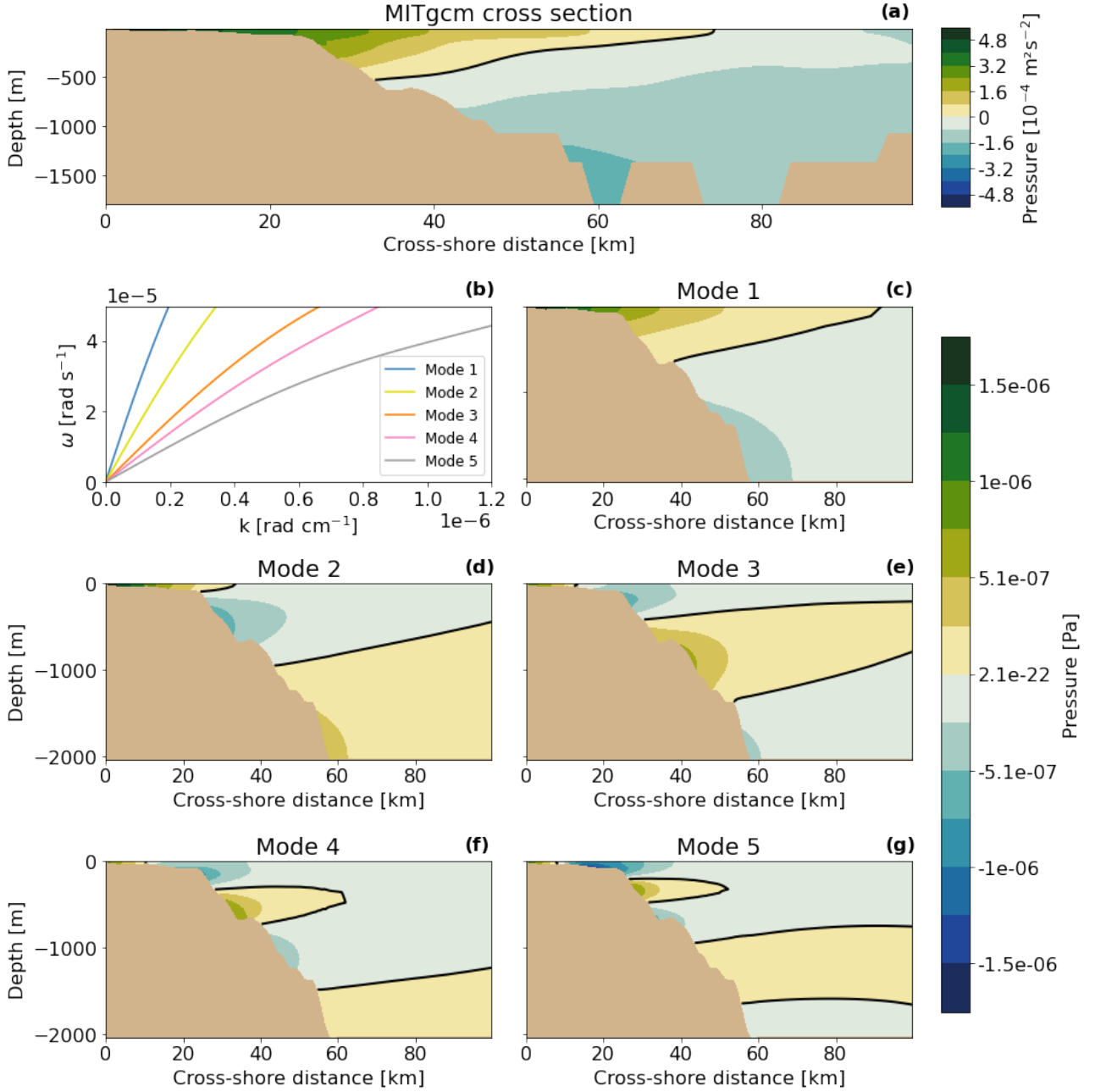
Figure 6: Vertical cross sections at 30.7°N from (a) the MITgcm model at time 2 days and (c)-(g) the first 5 modes found in the CTW model, in (b) are their corresponding dispersion curves. In a and c-g black lines mark zero-crossings. The coastline in the output from the coastal trapped wave model ((c)-(g)) has been smoothed from 60 km from the bay due to the required flat bottom at the open boundary in the CTW model, see section 2.2.

Table 1: The resulting characteristics of the waves found in the linear CTW model, first 7 columns, for modes 0-6, and in the MITgcm model in column 8 for depth 480 m and in column 9 for surface values. They are shown for 4 locations at the coast, 30, 31.40, 32 and 32.68°N

	Mode 0	Mode 1	Mode 2	Mode 3	Mode 4	Mode 5	Mode 6	MITgcm At depth 480 m	MITgcm At surface
30°N									
Wavenumber (rad/cm)	5.19E-08	2.02E-07	2.27E-07	3.03E-07	5.19E-09	5.19E-07		3.42E-07	1.50E-07
Wavelength (km)	1209.6	311.04	276.48	207.36	12096	120.96		183.57	420.13
Angular frequency (rad/s)	7.29E-05	6.02E-05	3.22E-05	2.89E-05	3.77E-07	3.45E-05		6.36E-05	6.36E-05
Period (days)	1.00	1.21	2.26	2.52	192.72	2.11		1.14	1.14
Phase speed (m/s)	14.04	2.98	1.42	0.95	0.73	0.67		1.86	4.25
31.40°N									
Wavenumber (rad/cm)	9.09E-08	2.02E-07	3.64E-07	4.55E-07	5.59E-07	7.27E-07		2.81E-07	2.91E-07
Wavelength (km)	691.20	311.04	172.80	138.24	112.32	86.40		223.97	216.15
Angular frequency (rad/s)	7.60E-05	4.32E-05	3.59E-05	3.65E-05	3.44E-05	3.75E-05		6.36E-05	6.36E-05
Period (days)	0.96	1.68	2.02	1.99	2.12	1.94		1.14	1.14
Phase speed (m/s)	8.36	2.14	0.99	0.80	0.61	0.52		2.27	2.19
32°N									
Wavenumber (rad/cm)	9.09E-08	2.02E-07	3.64E-07	4.55E-07		7.27E-07		6.43E-07	2.53E-07
Wavelength (km)	691.20	311.04	172.80	138.24		86.40		97.68	248.37
Angular frequency (rad/s)	7.60E-05	4.32E-05	3.59E-05	3.65E-05		3.75E-05		6.36E-05	6.36E-05
Period (days)	0.96	1.68	2.02	1.99		1.94		1.14	1.14
Phase speed (m/s)	8.36	2.14	0.99	0.80		0.52		0.99	2.52
32.68°N									
Wavenumber (rad/cm)	9.09E-08	2.02E-07	2.60E-07	4.55E-07	6.06E-09	9.09E-07	7.27E-07	1.28E-07	3.86E-07
Wavelength (km)	691.20	311.04	241.92	138.24	10368.00	69.12	86.40	488.99	162.64
Angular frequency (rad/s)	7.94E-05	4.10E-05	2.68E-05	2.95E-05	3.64E-07	3.27E-05	1.09E-05	6.36E-05	6.36E-05
Period (days)	0.92	1.78	2.71	2.47	2.59	2.23	6.67	1.14	1.14
Phase speed (m/s)	8.74	2.03	1.03	0.65	0.60	0.36	0.15	4.95	1.65

3.3   Composition analysis

The linear regression was performed at all timesteps at eight cross-sections along the coast and on average showed that around 98 % of the variation in the MITgcm model output can be explained by the first 4 modes. At some locations, more modes were allowed in the linear model but the addition of these modes did not significantly increase the success of the fit. The fit shows that the dominant mode is mode 1 and the weight of the mode decreases with increasing modal number (figure 7).
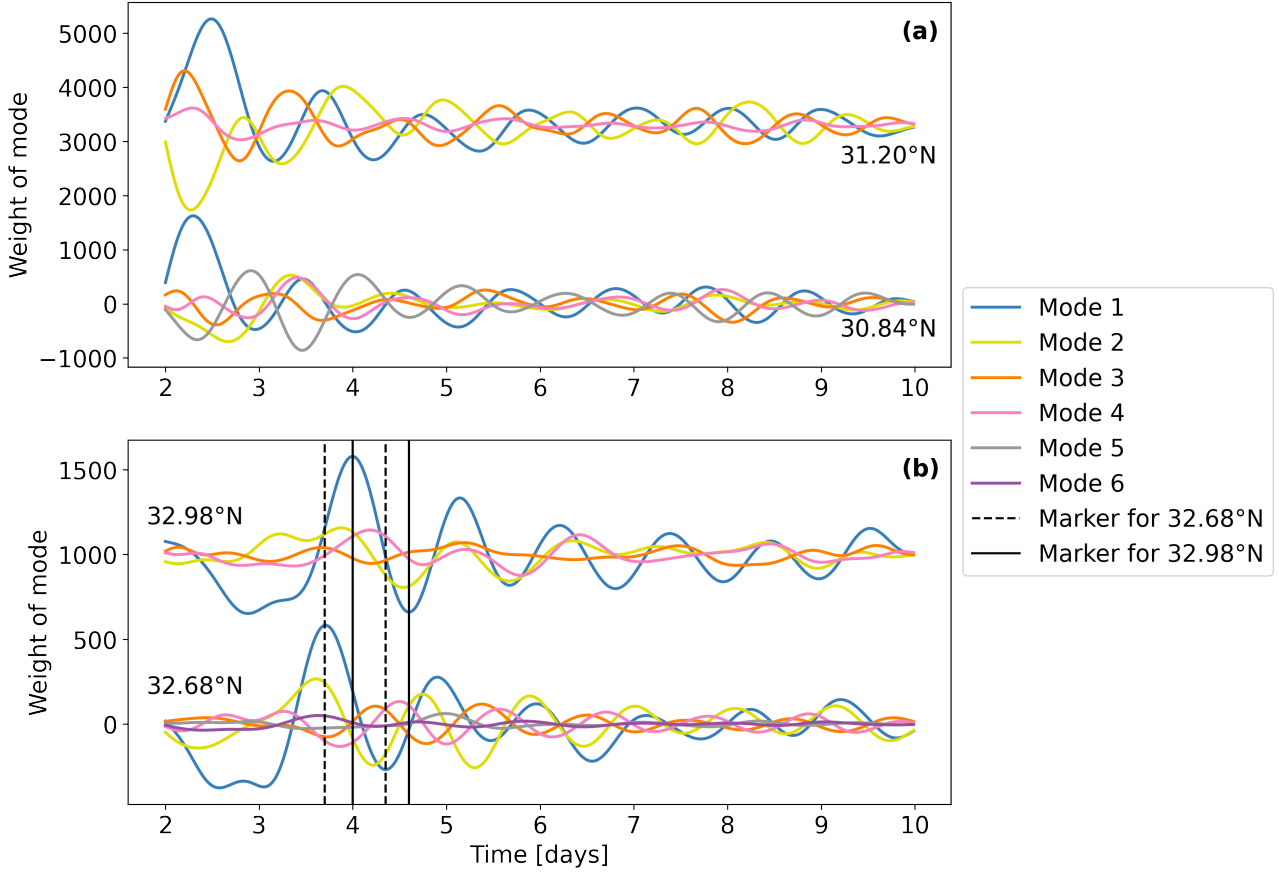
Figure 7: The weight of each mode for the output equation from the linear regression. At latitudes (a) 30.84, 31.20, (b) 32.68 and 32.98 °N. The lines for 31.20 (a) and 32.98°N (b) have been offset by 3300 and 1000 respectively, allowing them to be visualised in the same plot as the other location. In (b) vertical lines mark the time and thus shows modal configuration for the vertical structures in figure 8a-b (dashed lines) and figure 9a-b (solid lines).

For the eight cross-sections, the weight of each mode over time was evaluated. This analysis showed that the weight of the modes varies periodically, the weight decrease over time and that at locations further north the stable oscillation between dominant modes begins later than further south. These results can be seen in figure 7 as it presents the evolution of the mode weights for the cross-sections marked out in figure 3. At the latitudes further north the weight is overall lower than further south. For each time in figure 7, and thus for each combination of modes, we have a corresponding output in MITgcm, on which the linear regression has been performed. The modal structures corresponding to latitudes 32.68 and 32.98°N are shown in figures 8 and 9. They are shown alongside two cross-sections from MITgcm both at locations where mode 1 dominates, first in-phase and the next in anti-phase, see the composition of modes at these locations as dashed (32.68°N) and solid (32.98°N) black lines in figure 7.
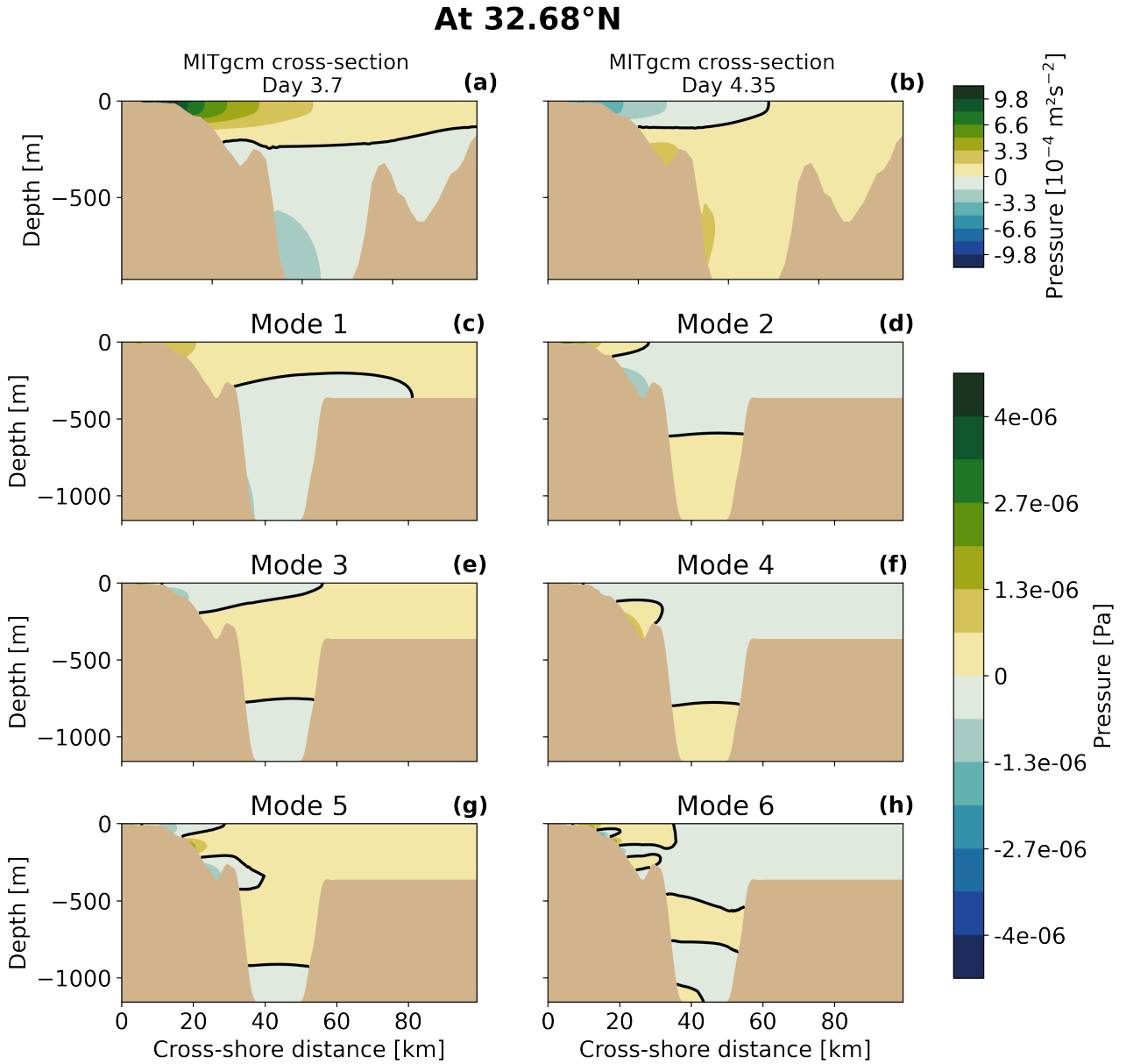
Figure 8: Vertical cross sections at 32.68°N from the MITgcm model after 3.7 (a) and 4.35 days (b) corresponding to the dashed lines showing the configuration of modal weights in figure 7. The vertical structure of these modes, from the CTW model, is shown in (c)-(h). Black lines mark zero-crossings. The coastline in the output from the coastal trapped wave model ((c)-(g)) has been smoothed from around 60 km from the bay due to the required flat bottom at the open boundary in the CTW model, see section 2.2.

The differences in topography between 32.68 and 32.98°N are that 32.68°N has a larger shelf width and does not decrease in depth monotonically from the coast while at 32.98°N the shelf is barely present. This presents very different propagation conditions for the CTWs, and this can be shown in the variation of mode structure. The behaviour of the wave in the presence of the shelf is very barotropic (figure 8) and bottom trapping does not occur on modes lower than mode 4. Without a shelf, the wave displays stronger bottom tapping beginning at mode 2 (figure 9). At 32.68°N more modes were allowed which could be due to the double shelf [Brink,
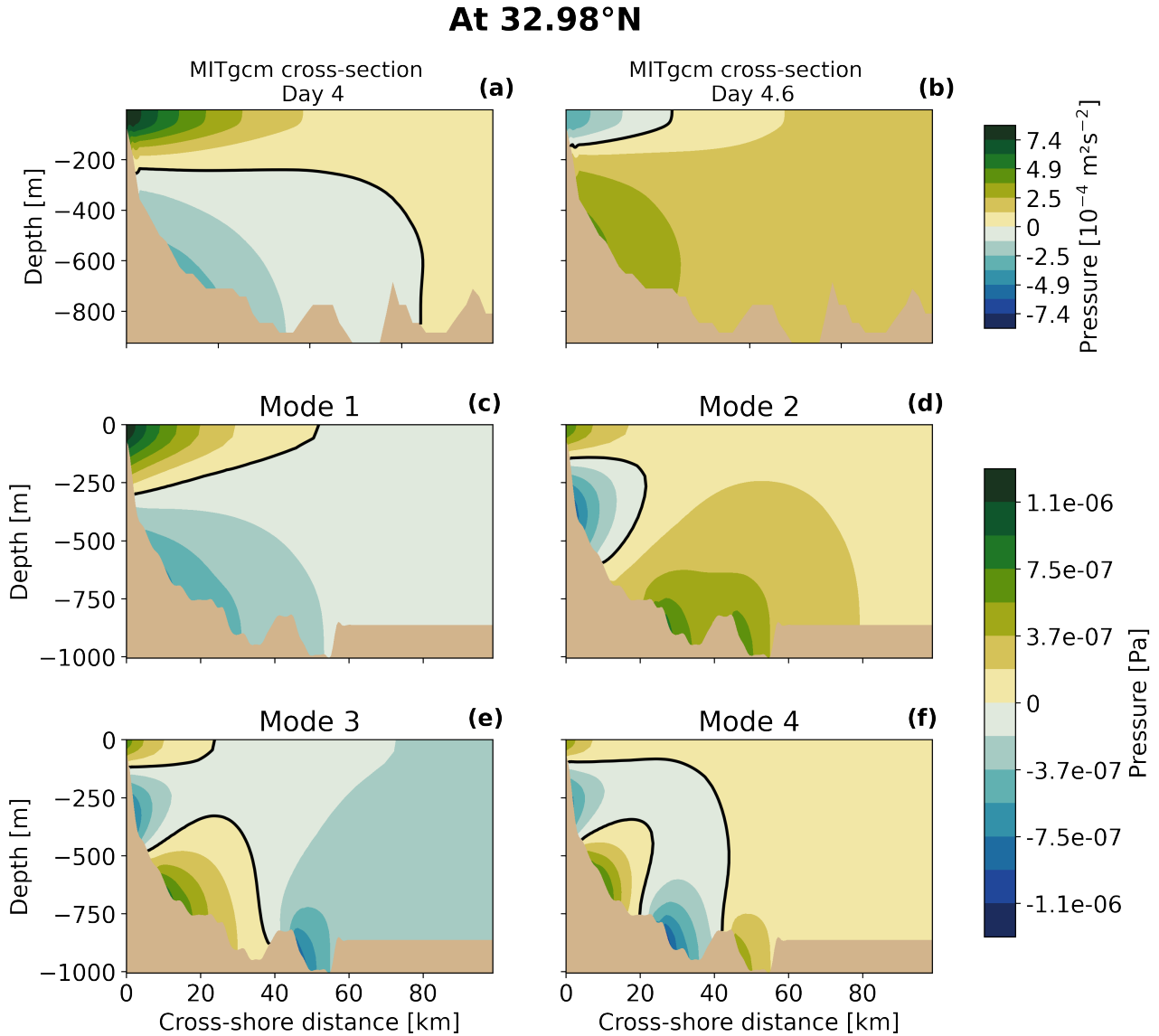
Figure 9: Vertical cross sections at 32.98°N from the MITgcm model after 4 (a) and 4.6 days (b) corresponding to the solid lines showing the configuration of modal weights in figure 7. The vertical structure of these modes, from the CTW model, is shown in (c)-(h). Black lines mark zero-crossings. The coastline in the output from the coastal trapped wave model ((c)-(g)) has been smoothed from around 60 km from the bay due to the required flat bottom at the open boundary in the CTW model, see section 2.2.

4 Discussion

Throughout this project, a methodology has been developed to characterise the coastal trapped waves generated following a short wind event over Sebastián Vizcaíno Bay. The characteristics of these waves have been analysed through both a circulation model, MITgcm, and a linear model, compiled by Brink [2018]. From these different methods, we can see not only

the general signal and the properties of the CTW propagation but also their characteristics when decomposed into separate linear modes. We know that the first four modes can be used to successfully represent the vertical structure of CTWs generated in the bay. The character of the linear model lets us calculate the properties of these modes at a coastline with a specific topographic structure no matter the origin of the wave. Knowing this the information extracted for the modes is not only useful for CTWs propagating from the SVB but also for CTWs generated due to other phenomena further south such as El Niño or equatorial waves.

The proficiency of the linear CTW model was assessed for this particular and realistically varying coastline. Comparing the resulting characteristics of waves output from this model to the waves generated in the MITgcm model there is a general agreement as was expected [Musgrave, 2019]. The models show similar values of phase speed, period and wavelength. The modal structures generated by the linear CTW model were successfully used to describe the vertical structure of the wave in the circulation model. From this, we learned that the first mode dominates, and the weight of the modes decreases with the mode number. This explains why the characteristics of the higher modes, above 3, deviate, eg. they are slower and thus have a longer period, compared to the CTWs in the circulation model. As we begin the analysis on the second day after the initial wind burst the barotropic mode was deemed too fast to be analysed, with its phase speed of 8 m/s (29 km/h, meaning it would take about 1.5 days to travel the whole domain of 1000 km).

A circulation model was created to investigate how bathymetry affects the area's physical processes, which means that many other parameters were set to not vary over the domain. Any variation in the CTWs present can then be expected to be generated due to changes in bathymetry, or a change in the Coriolis parameter. The Coriolis parameter increases further north which should indicate an increase in phase speed, but this is not seen in the results where we instead see a decrease. As mentioned by Enfield and Allen [1983] this can be due to the influence of the bottom topography off the coast of Baja California. Therefore it can be stated that the bottom topography has a larger impact on the propagation characteristics of the waves than the Coriolis parameter at this location. Significant variations in the propagation of the waves, as seen in figure 3a, were thus assumed to be due to changes in topography leading to a further investigation of the topography around these areas.

Indeed abrupt changes in CTW behaviour coincided with abrupt changes in topography (figures 3c and d). Two areas were chosen to be investigated further due to this. The first is between 30.84 and 31.20°N where the change in topography shows a decrease in total offshore depth and the second is between 32.68 and 32.98°N where the shelf quickly narrows (figure 3d). These changes were not only connected with changes in CTW phase speed (figures 3a and b) but also in energy distribution (figure 5) and the configuration and structure of allowed modes (figures

20

6, 7, 8 and 9). In these areas, both internal phase speed and PSD decreases locally (figures 2a, 5a), meaning that we see a reduction in power at the strongest frequency, $1/1.1$ days^{-1}, as the shelf topography changes. When the energy decreases at the strongest frequency there is an increase in power at a frequency of $1/4$ days^{-1}, suggesting that energy has been transferred into a wave mode with this dominant frequency. After this so-called disturbance in the shelf, there is a return of power in the dominating frequency and a decrease at the other, suggesting the waves return to their previous propagation behaviour.

The weight distribution between the modes (figure 7) indicates that changes in topography initiate a displacement of energy into lower modes as both the locations after a topographical variation have fewer allowed modes than the one before. The modes that disappear are the higher modes which are contradictive to the decrease in phase speed, as higher modes are associated with lower phase speed. It is also of interest to point out that at locations such as 32.68°N (figure 8) where the depth decreases away from the coast after an increase in depth, the linear CTW model could be generating a signal similar to what is found in the presence of a trench. Thus, the CTW model allows an infinite number of trapped waves to propagate in both directions [Brink, 1991] this could be a reason for the higher number of modes at this location. This topographic feature and the other detailed topographies used in the linear model could be a source of error as there is reason to assume that they are stretching the limits of the model's performance. It would be of interest to further understand the model's performance under these circumstances as previous investigations are used on more simplified topography [Eg. Lüdke et al., 2020, Brunner et al., 2019, Masoud et al., 2019, Battisti and Hickey, 1984].

The characteristics of coastal trapped waves have been shown to be significantly affected by bottom topography and idealized experiments have been performed to classify the impact of certain circumstances, such as changes in shelf width [Zhang and Yankovsky, 2016, Wilkin and Chapman, 1987], the relation between shelf width and total depth [Schulz et al., 2012], general irregularities in stratified [Wilkin and Chapman, 1990] and barotropic ocean [Wang, 1980]. The resulting behaviour of the CTWs in these reports cannot be directly compared to the result in this current study where the behaviour of the coastline is not as simple. Instead, it allows for certain variations, and their potential influence on the wave, to be discussed.

According to findings by Schulz et al. [2012] and Wilkin and Chapman [1990] a narrow shelf is associated with lower phase speed than that of a wide shelf. This agrees with the noted decrease in phase speed when the wave encounters a narrower shelf, eg. between 32.68 and 32.98°N (figure 3d). Other investigations of real in situ data have presented the same behaviour in CTWs [Woodham et al., 2013]. While this is true, many factors play a part and it is worth mentioning that the narrowing of shelves in a barotropic ocean has been associated with an increase in phase speed [Zhang and Yankovsky, 2016], which is the opposite of what was found in this work.

Generally, a change in deep ocean depth has not been shown to affect the behaviour of CTWs [Wilkin and Chapman, 1987] but it has been shown that increased total depth in comparison to the depth of the shelf can be associated with a lower phase speed [Schulz et al., 2012]. Thus indicating that the opposite, a shallower total depth, would increase the phase speed, which we did not see in the resulting behaviour of the CTWs between 30.84 and 31.20°N (figure 3d). But this may be caused by the friction starting to affect the wave significantly thus overpowering the effect of the bathymetry change [Enfield and Allen, 1983]. This disagreement may also be due to the lack of change in the slope between these points which may in fact play a larger role than the other changes in topography. The steepness of the slope is of great importance as the vorticity gradient is a central force in the propagation of CTWs [Schulz et al., 2012, Wilkin and Chapman, 1990], but there is lacking information on the exact impact of this.

There is a consensus that abrupt changes in topography induce the dispersion of CTWs, but depending on the type of topographical change the dispersion mechanisms vary. Because of this variation, it has been concluded to be of great importance to include CTW scattering when working with irregular coastlines to be able to correctly interpret the variation in physical processes [Wilkin and Chapman, 1990]. When the shelf changes width it induces energy fluxes across isobaths [Zhang and Yankovsky, 2016] and between modes, for example Wilkin and Chapman [1987] mentions that a widening of the shelf has been associated with energy transferring to higher modes. No information on the movement of energy between modes was found for the case of a narrowing shelf, but the results of this study suggest that a narrower shelf would transfer energy to lower modes.

The reason for the lack of information in the case of a narrowing shelf is that more of the wave energy is reflected, i.e. the scattering affects the behaviour of the wave upstream of the anomaly in topography [Wilkin and Chapman, 1990, Zhang and Yankovsky, 2016, Schulz et al., 2012]. Because of this phenomenon, the reaction of a CTW upon the narrowing of a shelf has been excluded from investigations of barotropic wave behaviour as the solution presents significant errors [Wilkin and Chapman, 1987]. In reports including stratification, the distribution of modes has not been mentioned thoroughly either. It is assumed to be because even though stratified waters are expected to dampen this reflection it has been shown that there is still a large influence of backscattering of the wave [Wilkin and Chapman, 1990, Zhang and Yankovsky, 2016].

The presence of backscattering at the locations of narrowing shelves has been associated with an increased across-shelf flow upstream from the narrowing of the shelf [Wilkin and Chapman, 1990, Zhang and Yankovsky, 2016]. Scattering of CTWs is a phenomenon happening at all the previously discussed abrupt topographical changes and all cases have been associated with increases in cross-shore transport and thus upwelling [Wang, 1980]. At locations where the depth

does not increase monotonically away from the coast we would see similar behaviour to that of CTWs encountering a trench or canyon [Brink, 1991]. This type of topographical change has previously been shown to induce upwelling and increased onshore flow [Saldías et al., 2021]. The complicated topography in the Southern California Bight likely induces this scattering phenomenon and it is here that the waves cease to be distinguishable (figure 3a-c). The dispersion of the waves in this area could be one of the many processes increasing the upwelling in this particular area of the CCS.

The ability of the numerical solution in the linear model [Brink, 2018] to take this scattering into account is of high interest and the capacity of this model has been evaluated previously by Brunner et al. [2019]. The purpose of their study was to evaluate the then currently available analytical linear solutions for CTWs in stratified waters, with bottom friction but most importantly complex bottom topography. They investigate the success of predictions made using analytical models created by Brink [2006] and Gill and Schumann [1974] in taking CTW scattering into account. The conclusion is that, since Brink [2006] calculates the waves for a bathymetry homogenous in the alongshore direction it is unable to take factors induced by abrupt changes in topography, like the ones mentioned in the previous paragraphs, into account. Thus, Brunner et al. [2019] concluded that the linear models still are not refined enough to effectively be applied on high scattering regions.

Another result of interest presented by Brunner et al. [2019] is that of the influence of friction and stratification which our current investigation has not covered. They mention that stratification is not of high importance for the propagation of CTWs in their location of research but that wind forcing and friction are the main affecting factors, beyond topography changes. When including friction in their model Brunner et al. [2019] note a large change in decay times, especially for mode 1 which isn't usually the mode most affected by the dampening of bottom friction [Zhang and Yankovsky, 2016]. They also argue against previous theories that suggest a decrease in scattering due to friction as Brunner et al. [2019] found a presence of higher modes. The importance of stratification is not fully agreed upon as other studies, for example Wilkin and Chapman [1990] indicate that increased stratification can enhance scattering and guide more energy into higher modes. It would be of interest to investigate the effect of these parameters on the behaviour of CTWs generated by the SVB.

When comparing the linear model with the results of the MITgcm model there is some caution that needs to be taken into account. Most of the errors are assumed to be originating from the complex topography, which the linear CTW model requires to be smoothed while the MITgcm model maintains more details. Therefore when interpolating the values from the linear model to be comparable to that of the circulation model there is room for error. It would be useful to perform a more refined fit of these two outputs, for example, a regularised and weighted multi-

variate linear regression, where the areas disturbed by the discrepancies in topography could be accounted for. Although it would be interesting to decrease the smoothing in the linear model, this would be done apprehensively as the topography potentially already is too complex even at the current level of smoothing. Another way of equating them would be to further smooth the input bathymetry in the MITgcm model, although this would negate the purpose of the current investigation as preliminary runs have shown that smoothing of the topography has a large impact on wave propagation. It may still be a worthwhile investigation to understand where the models differ.

To summarise, coastal trapped waves generated by the presence of Sebastián Vizcaíno Bay propagate along the coast of California up to the Southern California Bight. They are affected by topography changes but can reestablish their propagation pattern after disturbances. In the SCB they dissipate but due to the uncertainty in their behaviour, they may reestablish further north of the investigated domain. This dissipation leads to energy displacement which in turn is associated with mixing in the area. When meeting certain topographical changes the dissipation can also lead to an increased cross-shore flow. This cross-shore flow and general mixing play a part in the surfacing of oxygen-depleted and nutrient-rich bottom water seen in the SCB.

5 Conclusion and outlook

I have in this project produced a methodology for the classification of coastal trapped waves propagating along the coast of northern Baja California up to the Southern California Bight. The theory combines a general circulation model with linear theory both working on inputs of real bathymetry. It is of great importance that these waves can be characterised correctly as they are central in upwelling processes in the CCS and could be generating significant across-shore transport in the SCB.

Solving for the linearized solution of the CTWs at a number of locations along the coast, presenting different topographical features, the modal composition of the waves and how it is affected by topographical changes was determined. It was shown that the waves can be recreated with an adequate agreement to those presented in the circulation model from the first four modal structures. Even though abrupt topographical changes could lead to a variance that the linear model cannot take into account, it has been noted that the waves tend to rebalance themselves and the vertical structures are still comparable. In theory, these changes in topography should lead to scattering, which could mean that energy loss may need to be accounted for, as well as energy being displaced to other modal structures.

In future studies, it would be of interest to investigate the response the waves have to realistic variations in stratification, friction and wind forcing, as well as compare the resulting physical responses to in situ measurements. Along with these tests, a new investigation of the agreement between the linear model and the MITgcm model could be developed. It would be particularly interesting to develop a model in MITgcm to work similarly to that of the linear CTW model [Brink, 2018], which could be done by simply smoothing the coastline or going the next step and creating a coastline uniform in the alongshore direction. The purpose of this would be to understand further where the linear model potentially diverges from the model created in MITgcm.

6   References

Alberto Amador-Buenrostro, Maria Luisa Argote-Espinosa, Manuel Mancilla-Peraza, and Manuel Figueroa-Rodríguez. Short-Term Variations of the Anticyclonic Circulation in Bahía Sebastián Vizcaíno, BC. *Ciencias Marinas*, 21(2):201–223, Mar. 1995. doi: 10.7773/cm.v21i2. 987. URL https://cienciasmarinas.com.mx/index.php/cmarinas/article/view/987. 1

David S. Battisti and Barbara M. Hickey. Application of Remote Wind-Forced Coastal Trapped Wave Theory to the Oregon and Washington Coasts. *Journal of Physical Oceanography*, 14(5):887 – 903, 1984. doi: 10.1175/1520-0485(1984)014⟨0887:AORWFC⟩2.0.CO; 2. URL https://journals.ametsoc.org/view/journals/phoc/14/5/1520-0485_1984_014_0887_aorwfc_2_0_co_2.xml. 3, 6, 21

Kenneth H. Brink. Coastal-Trapped Waves and Wind-Driven Currents Over the Continental Shelf. *Annual Review of Fluid Mechanics*, 23(1):389–412, 1991. doi: 10.1146/annurev.fl.23. 010191.002133. URL https://doi.org/10.1146/annurev.fl.23.010191.002133. 2, 3, 18, 21, 23

Kenneth H. Brink. Coastal-Trapped Waves with Finite Bottom Friction. *Dynamics of Atmospheres and Oceans*, 41(3):172–190, 2006. ISSN 0377-0265. doi: https://doi.org/10.1016/j.dynatmoce.2006.05.001. URL https://www.sciencedirect.com/science/article/pii/S0377026506000212. 23

Kenneth H. Brink. Stable Coastal-Trapped Waves with Stratification, Topography and Mean Flow, Aug 2018. URL https://hdl.handle.net/1912/10527. 3, 6, 19, 23, 25

Kelsey Brunner, David Rivas, and Kamazima M. M. Lwiza. Application of Classical Coastal Trapped Wave Theory to High-Scattering Regions. *Journal of Physical Oceanography*, 49 (9):2201 – 2216, 2019. doi: 10.1175/JPO-D-18-0112.1. URL https://journals.ametsoc.org/view/journals/phoc/49/9/jpo-d-18-0112.1.xml. 3, 6, 21, 23

Allan J. Clarke and Kenneth H. Brink. The Response of Stratified, Frictional Flow of Shelf and Slope Waters to Fluctuating Large-Scale, Low-Frequency Wind Forcing. *Journal of Physical Oceanography*, 15(4):439 – 453, 1985. doi: 10.1175/1520-0485(1985)015⟨0439: TROSFF⟩2.0.CO;2. URL https://journals.ametsoc.org/view/journals/phoc/15/4/1520-0485_1985_015_0439_trosff_2_0_co_2.xml. 2

Francois Colas, Xavier J. Capet, James C. McWilliams, and Alexander F. Shchepetkin. 1997–1998 El Niño off Peru: A Numerical Study. *Progress in Oceanography*, 79(2):138–155, 2008. ISSN 0079-6611. doi: https://doi.org/10.1016/j.pocean.2008.10.015. URL https://www.sciencedirect.com/science/article/pii/S0079661108001687. 2

Thomas P. Connolly, Barbara M. Hickey, Igor Shulman, and Richard E. Thomson. Coastal Trapped Waves, Alongshore Pressure Gradients, and the California Undercurrent. *Journal of Physical Oceanography*, 44(1):319 – 342, 2014. doi: 10.1175/JPO-D-13-095.1. URL https://journals.ametsoc.org/view/journals/phoc/44/1/jpo-d-13-095.1.xml. 2

Changming Dong, Eileen Y. Idica, and James C. McWilliams. Circulation and Multiple-Scale Variability in the Southern California Bight. *Progress in Oceanography*, 82(3):168–190, 2009. ISSN 0079-6611. doi: https://doi.org/10.1016/j.pocean.2009.07.005. URL https://www.sciencedirect.com/science/article/pii/S0079661109000573. 1

David B. Enfield and John S. Allen. The Generation and Propagation of Sea Level Variability Along the Pacific Coast of Mexico. *Journal of Physical Oceanography*, 13(6):1012 – 1033, 1983. doi: 10.1175/1520-0485(1983)013⟨1012:TGAPOS⟩2.0.CO; 2. URL https://journals.ametsoc.org/view/journals/phoc/13/6/1520-0485_1983_013_1012_tgapos_2_0_co_2.xml. 2, 3, 6, 20, 22

Frauke Feser, Burkhardt Rockel, Hans von Storch, Jörg Winterfeldt, and Matthias Zahn. Regional Climate Models Add Value to Global Model Data: A Review and Selected Examples. *Bulletin of the American Meteorological Society*, 92(9):1181 – 1192, 2011. doi: 10.1175/2011BAMS3061.1. URL https://journals.ametsoc.org/view/journals/bams/92/9/2011bams3061_1.xml. 1

Howard Georgi. *The Physics of Waves*. Prentice Hall Englewood Cliffs, NJ, 1993. 2

Adrian E. Gill and Eckart H. Schumann. The Generation of Long Shelf Waves by the Wind. *Journal of Physical Oceanography*, 4(1):83 – 90, 1974. doi: 10.1175/1520-0485(1974)004⟨0083: TGOLSW⟩2.0.CO;2. URL https://journals.ametsoc.org/view/journals/phoc/4/1/1520-0485_1974_004_0083_tgolsw_2_0_co_2.xml. 23

GEBCO Compilation Group. *Gebco 2020 grid*, 2020. doi: 10.5285/a29c5465-b138-234d-e053-6c86abc040b9. 4

Barbara M. Hickey. The California Current System—Hypotheses and Facts. *Progress in Oceanography*, 8(4):191–279, 1979. ISSN 0079-6611. doi: https://doi.org/10.1016/0079-6611(79)90002-8. URL https://www.sciencedirect.com/science/article/pii/0079661179900028. 1

Chris W Hughes, Ichiro Fukumori, Stephen M Griffies, John M Huthnance, Shoshiro Minobe, Paul Spence, Keith R Thompson, and Anthony Wise. Sea Level and the Role of Coastal Trapped Waves in Mediating the Influence of the Open Ocean on the Coast. *Surveys in Geophysics*, 40(6):1467–1492, 2019. doi: 10.1007/s10712-019-09535-x. URL https://doi.org/10.1007/s10712-019-09535-x. 2

John M. Huthnance, Lawrence A. Mysak, and Dong-Ping Wang. *Coastal Trapped Waves*, chapter 1, pages 1–18. American Geophysical Union (AGU), 1986. ISBN 9781118664995. doi: https://doi.org/10.1029/CO003p0001. URL https://agupubs.onlinelibrary.wiley.com/doi/abs/10.1029/CO003p0001. 2

Jan Lüdke, Marcus Dengler, Stefan Sommer, David Clemens, Sören Thomsen, Gerd Krahmann, Andrew W. Dale, Eric P. Achterberg, and Martin Visbeck. Influence of Intraseasonal Eastern Boundary Circulation Variability on Hydrography and Biogeochemistry off Peru. *Ocean Science*, 16(6):1347–1366, 2020. doi: 10.5194/os-16-1347-2020. URL https://os.copernicus.org/articles/16/1347/2020/. 3, 6, 21

John Marshall, Alistair Adcroft, Chris Hill, Lev Perelman, and Curt Heisey. A Finite-Volume, Incompressible Navier Stokes Model for Studies of the Ocean on Parallel Computers. *Journal of Geophysical Research: Oceans*, 102(C3):5753–5766, 1997. doi: https://doi.org/10.1029/96JC02775. URL https://agupubs.onlinelibrary.wiley.com/doi/abs/10.1029/96JC02775. 3, 4

Mina Masoud, Rich Pawlowicz, and Masoud Montazeri Namin. Low Frequency Variations in Currents on the Southern Continental Shelf of the Caspian Sea. *Dynamics of Atmospheres and Oceans*, 87:101095, 2019. ISSN 0377-0265. doi: https://doi.org/10.1016/j.dynatmoce.2019.05.004. URL https://www.sciencedirect.com/science/article/pii/S0377026518301441. 3, 6, 21

Matthew R. Mazloff, Bruce Cornuelle, Sarah T. Gille, and Jinbo Wang. The Importance of Remote Forcing for Regional Modeling of Internal Waves. *Journal of Geophysical Research: Oceans*, 125(2):e2019JC015623, 2020. doi: https://doi.org/10.1029/2019JC015623. URL https://agupubs.onlinelibrary.wiley.com/doi/abs/10.1029/2019JC015623. e2019JC015623 10.1029/2019JC015623. 1

Sam McClatchie. *Regional Fisheries Oceanography of the California Current System*. Springer, 2016. 1

Julian P. McCreary and Michael James Lighthill. A Linear Stratified Ocean Model of the Coastal Undercurrent. *Philosophical Transactions of the Royal Society of London. Series A, Mathematical and Physical Sciences*, 302(1469):385–413, 1981. doi: 10.1098/rsta.1981.0176. URL https://royalsocietypublishing.org/doi/abs/10.1098/rsta.1981.0176. 2

Ruth C. Musgrave. Energy Fluxes in Coastal Trapped Waves. *Journal of Physical Oceanography*, 49(12):3061 – 3068, 2019. doi: https://doi.org/10.1175/JPO-D-18-0172.1. URL https://journals.ametsoc.org/view/journals/phoc/49/12/jpo-d-18-0172.1.xml. 3, 20

I Orlanski. A Simple Boundary Condition for Unbounded Hyperbolic Flows. *Journal of Computational Physics*, 21(3):251–269, 1976. ISSN 0021-9991. doi: https://doi.org/10.1016/0021-9991(76)90023-1. URL https://www.sciencedirect.com/science/article/pii/0021999176900231. 5

Pierrick Penven, Patrick Marchesiello, Laurent Debreu, and Jérome Lefevre. Software Tools for Pre-and Post-Processing of Oceanic Regional Simulations. *Environmental Modelling & Software*, 23(5):660–662, 2008. doi: 10.1016/j.envsoft.2007.07.004. 4

S. George H. Philander and Jong-Hwan. Yoon. Eastern Boundary Currents and Coastal Upwelling. *Journal of Physical Oceanography*, 12(8):862 – 879, 1982. doi: 10.1175/1520-0485(1982)012⟨0862:EBCACU⟩2.0.CO;2. URL https://journals.ametsoc.org/view/journals/phoc/12/8/1520-0485_1982_012_0862_ebcacu_2_0_co_2.xml. 2

James M. Pringle and Kristin Riser. Remotely Forced Nearshore Upwelling in Southern California. *Journal of Geophysical Research: Oceans*, 108(C4), 2003. doi: https://doi.org/10.1029/2002JC001447. URL https://agupubs.onlinelibrary.wiley.com/doi/abs/10.1029/2002JC001447. 1, 2

Karina Ramos-Musalem. High-Frequency Variability Induced in the Southern California Bight by a Wind Event in Sebastian Vizcaíno Bay, Baja California. *American Geophysical Union (AGU)*, Under review. 5

Gonzalo S. Saldías, Karina Ramos-Musalem, and Susan E. Allen. Circulation and Upwelling Induced by Coastal Trapped Waves Over a Submarine Canyon in an Idealized Eastern Boundary Margin. *Geophysical Research Letters*, 48(11):e2021GL093548, 2021. doi: https://doi.org/10.1029/2021GL093548. URL https://agupubs.onlinelibrary.wiley.com/doi/abs/10.1029/2021GL093548. 23

William J. Schulz, Richard P. Mied, and Charlotte M. Snow. Continental Shelf Wave Propagation in the Mid-Atlantic Bight: A General Dispersion Relation. *Journal of Physical Oceanography*, 42(4):558 – 568, 2012. doi: 10.1175/JPO-D-11-098.1. URL https://journals.ametsoc.org/view/journals/phoc/42/4/jpo-d-11-098.1.xml. 21, 22

Richard E. Thomson and William J. Emery. Chapter 3 - Statistical Methods and Error Handling. In *Data Analysis Methods in Physical Oceanography*, pages 219–311. Elsevier, Boston, third edition, 2014. ISBN 978-0-12-387782-6. doi: https://doi.org/10.1016/B978-0-12-387782-6.00003-X. URL https://www.sciencedirect.com/science/article/pii/B978012387782600003X. 8

Ariane Verdy, Matthew R. Mazloff, Bruce D. Cornuelle, and Sung Yong Kim. Wind-Driven Sea Level Variability on the California Coast: An Adjoint Sensitivity Analysis. *Journal of Physical Oceanography*, 44(1):297 – 318, 2014. doi: 10.1175/JPO-D-13-018.1. URL https://journals.ametsoc.org/view/journals/phoc/44/1/jpo-d-13-018.1.xml. 1, 2

Dong-Ping Wang. Diffraction of Continental Shelf Waves by Irregular Alongshore Geometry. *Journal of Physical Oceanography*, 10(8):1187 – 1199, 1980. doi: 10.1175/1520-0485(1980)010⟨1187:DOCSWB⟩2.0.CO;2. URL https://journals.ametsoc.org/view/journals/phoc/10/8/1520-0485_1980_010_1187_docswb_2_0_co_2.xml. 21, 22

Dong-Ping Wang and Christopher N. K. Mooers. Coastal-Trapped Waves in a Continuously Stratified Ocean. *Journal of Physical Oceanography*, 6(6):853 – 863, 1976. doi: 10.1175/1520-0485(1976)006⟨0853:CTWIAC⟩2.0.CO;2. URL https://journals.ametsoc.org/view/journals/phoc/6/6/1520-0485_1976_006_0853_ctwiac_2_0_co_2.xml. 2

John L. Wilkin and David C. Chapman. Scattering of Continental Shelf Waves at a Discontinuity in Shelf Width. *Journal of Physical Oceanography*, 17(6):713 – 724, 1987. doi: 10.1175/1520-0485(1987)017⟨0713:SOCSWA⟩2.0.CO;2. URL https://journals.ametsoc.org/view/journals/phoc/17/6/1520-0485_1987_017_0713_socswa_2_0_co_2.xml. 21, 22

John L. Wilkin and David C. Chapman. Scattering of Coastal-Trapped Waves by Irregularities in Coastline and Topography. *Journal of Physical Oceanography*, 20(3):396 – 421, 1990. doi: 10.1175/1520-0485(1990)020⟨0396:SOCTWB⟩2.0.CO;2. URL https://journals.ametsoc.org/view/journals/phoc/20/3/1520-0485_1990_020_0396_soctwb_2_0_co_2.xml. 21, 22, 23

Robert Woodham, Gary B. Brassington, Robin Robertson, and Oscar Alves. Propagation Characteristics of Coastally Trapped Waves on the Australian Continental Shelf. *Journal of Geophysical Research: Oceans*, 118(9):4461–4473, 2013. doi: https://doi.org/10.1002/jgrc.20317. URL https://agupubs.onlinelibrary.wiley.com/doi/abs/10.1002/jgrc.20317. 2, 21

John G Wyllie. The Water Masses of Sebastian Vizcaino Bay. *CalCOFI Rep*, 8:83–93, 1961. 1

Katherine D. Zaba, Peter J. S. Franks, and Mark D. Ohman. The California Undercurrent as a Source of Upwelled Waters in a Coastal Filament. *Journal of Geophysical Research:*

Oceans, 126(2):e2020JC016602, 2021. doi: https://doi.org/10.1029/2020JC016602. URL https://agupubs.onlinelibrary.wiley.com/doi/abs/10.1029/2020JC016602. 2

Luis Zamudio, Harley E. Hurlburt, E. Joseph Metzger, and Ole Martin Smedstad. On the Evolution of Coastally Trapped Waves Generated by Hurricane Juliette Along the Mexican West Coast. *Geophysical Research Letters*, 29(23):56–1–56–4, 2002. doi: https://doi.org/ 10.1029/2002GL014769. URL https://agupubs.onlinelibrary.wiley.com/doi/abs/10. 1029/2002GL014769. 2

Tianyi Zhang and Alexander E Yankovsky. On the Nature of Cross-Isobath Energy Fluxes in Topographically Modified Barotropic Semidiurnal Kelvin Waves. *Journal of Geophysical Research: Oceans*, 121(5):3058–3074, 2016. doi: https://doi.org/10.1002/2015JC011617. URL https://agupubs.onlinelibrary.wiley.com/doi/abs/10.1002/2015JC011617. 21, 22, 23